ADVANCED FUNCTIONAL MATERIALS
www.afm-journal.de

www.MaterialsViews.com

Co-Percolating Graphene-Wrapped Silver Nanowire Network for High Performance, Highly Stable, Transparent Conducting Electrodes

Ruiyi Chen, Suprem R. Das, Changwook Jeong, Mohammad Ryyan Khan, David B. Janes, and Muhammad A. Alam**

Transparent conducting electrodes (TCEs) require high transparency and low sheet resistance for applications in photovoltaics, photodetectors, flat panel displays, touch screen devices and imagers. Indium tin oxide (ITO), or other transparent conductive oxides, have typically been used, and provide a baseline sheet resistance (R_S) vs. transparency (T) relationship. However, ITO is relatively expensive (due to limited abundance of Indium), brittle, unstable, and inflexible; moreover, ITO transparency drops rapidly for wavelengths above 1000 nm. Motivated by a need for transparent conductors with comparable (or better) R_S at a given T, as well as flexible structures, several alternative material systems have been investigated. Single-layer graphene (SLG) or few-layer graphene provide sufficiently high transparency (≈97% per layer) to be a potential replacement for ITO. However, large-area synthesis approaches, including chemical vapor deposition (CVD), typically yield films with relatively high sheet resistance due to small grain sizes and high-resistance grain boundaries (HGBs). In this paper, we report a hybrid structure employing a CVD SLG film and a network of silver nanowires (AgNWs): R_S as low as 22 Ω/□ (stabilized to 13 Ω/□ after 4 months) have been observed at high transparency (88% at $\lambda = 550$ nm) in hybrid structures employing relatively low-cost commercial graphene with a starting R_S of 770 Ω/□. This sheet resistance is superior to typical reported values for ITO, comparable to the best reported TCEs employing graphene and/or random nanowire networks, and the film properties exhibit impressive stability under mechanical pressure, mechanical bending and over time. The design is inspired by the theory of a co-percolating network where conduction bottlenecks of a 2D film (e.g., SLG, MoS_2) are circumvented by a 1D network (e.g., AgNWs, CNTs) and vice versa. The development of these high-performance hybrid structures provides a route towards robust, scalable and low-cost approaches for realizing high-performance TCE.

1. Introduction

Networks of silver nanowires (AgNWs nanonet) and single-wall carbon nanotubes (SWCNTs nanonet) have been investigated as potential replacements for ITO.[1–6] For NW or CNT densities corresponding to 85–95% transparency (T), conduction in these networks is typically dominated by percolation through junctions with relative large tube-tube/NW-NW contact resistance ($R_{NW\text{-}NW}$),[7–9] resulting in a rapid increase in baseline sheet resistance (R_S) (kΩ/□ -GΩ/□, depending on the NW/NT[4]) as T increases. Approaches involving welding of the nanowires,[10] thermal annealing under pressure,[11] or electroplating[4] decrease R_S[12] by improving $R_{NW\text{-}NW}$, but it has been challenging to reduce overall R_S below ≈30 Ω/□,[13] especially for broadband T at 90%. Moreover, micrometer-sized holes within the network add series resistance to devices that rely on vertical current transport such as LEDs and solar cells. Composite transparent conducting electrodes (TCEs) employing silver NWs with another conducting polymer such as PEDOT:PSS and a combination of TiO_2 nanoparticles with PEDOT:PSS have recently been demonstrated with sheet resistances of 12 Ω/□ at average T of 86% over wavelengths 350–800 nm and 15 Ω/□ at T_{550nm} of 83% respectively.[14,15] The conducting polymer and TiO_2 nanoparticle

R. Chen, C. Jeong, M. R. Khan, Prof. D. B. Janes, Prof. M. A. Alam
School of Electrical and Computer Engineering
Purdue University
West Lafayette, IN 47907, USA
E-mail: janes@ecn.purdue.edu; alam@ecn.purdue.edu
S. R. Das
Department of Physics
Purdue University
West Lafayette, IN 47907, USA

S. R. Das, Prof. D. B. Janes
Birck Nanotechnology Center
Purdue University
West Lafayette, IN 47907, USA
R. Chen
Department of Information Science and Electronic Engineering
Zhejiang University
Hangzhou, 310027, China

DOI: 10.1002/adfm.201300124

primarily reduce the tube-tube contact resistance. Graphene, including single layer (SLG) and few-layer (FLG), has also been studied as a transparent conductor. 'Single-crystal' graphene, such as that obtained by exfoliation from highly ordered pyrolytic graphite (HOPG) crystals, exhibits several interesting physical phenomena,[16–21] including an R_S lower than ITO, at a given optical transparency. However, the exfoliated approach yields samples that are too small for practical applications. Large-area, polycrystalline, SLG sheets can be achieved by chemical-vapor deposition (CVD), typically involving growth on copper foil and subsequent transfer to an arbitrary substrate,[22–24] with grain sizes typically ranging from a few micrometers[25,26] to a few tens of micrometers,[27] depending on the specific growth conditions. There is an increasing effort to fundamentally understand the structure of graphene grain-boundaries (GBs) and the impact of GBs on mechanical strength as well as electronic transport.[25,26–32] Earlier, we classified the GBs broadly into two categories, namely high resistance grain-boundaries (HGBs) and low resistance grain-boundaries (LGBs), consistent with the transport gaps and high transmission proposed by Yazyev and Louie.[31,32] As illustrated in **Figure 1** (see Figure 1B), both HGBs and LGBs contribute to the resistance in a SLG film. The HGBs severely limit the (percolating) electronic transport, as indicated by best reported R_S of ≈250–700 Ω/□ (and 2–6 kΩ/□ for each layer in typical SLG/FLG). In typical CVD graphene grown on copper with average grain size of ≈1μm, we have recently estimated the percentage of HGBs by using percolation theory through HGBs[32] to interpret the resistance of circular transfer length measurement (CTLM) devices.[33] A number of groups have proposed methods or reported initial experimental results for improving the transport properties by GB engineering or doping.[26,32,34,35] CVD grown under high methane flow rate provides very uniform coverage over the copper foil and better inter-domain stitching, allowing control of R_S.[26] While the inter-grain four-terminal R_S changes between ≈3–9 kΩ as the carrier density is modulated, the intra-grain resistance scales up by a constant factor of 1.4 for the same modulation in carrier density, indicating scattering by GBs even for best quality poly-SLG. The most impressive result to date involved large scale CVD graphene by roll-to-roll production, in which the as-grown SLG R_S (≈250 Ω/□) was reduced to ≈125 Ω/□ by wet-chemical doping, and four layers were stacked to provide 30 Ω/□ at 90% transparency and at 550 nm (T_{550nm}≈90%).[36] Note that the chemical doping decreases R_S only by a factor of 2, because while conductivity of individual grain is enhanced, the percolating resistance is still dominated by the HGBs (Figure 1B). With this insight, we have previously explored the notion of 'percolation-doping':[32] in this approach, the R_S of graphene network is reduced not by increasing carrier density (as in chemical doping), but by opening up new conduction channels by bridging the HGBs with nanowires or nanotubes. Although most of the experiments based on solution-processed hybrid graphene/NW systems have not achieved R_S/ T relationships predicted by the theory,[32] nor performance comparable to that of ITO, a recent report by Kholmanov et. al.[35] has been encouraging: it achieved a R_S of 64 Ω/□ (24 Ω/□) at T_{550nm}≈90% using a sparse array of AgNWs and one (two) layer(s) of SLG. This experiment employed high quality graphene with relatively large grains (grain size ≈10–12 μm), and a NW density below the percolation limit. For these parameters, the improved R_S (with respect to that of SLG) can be attributed to percolation doping.

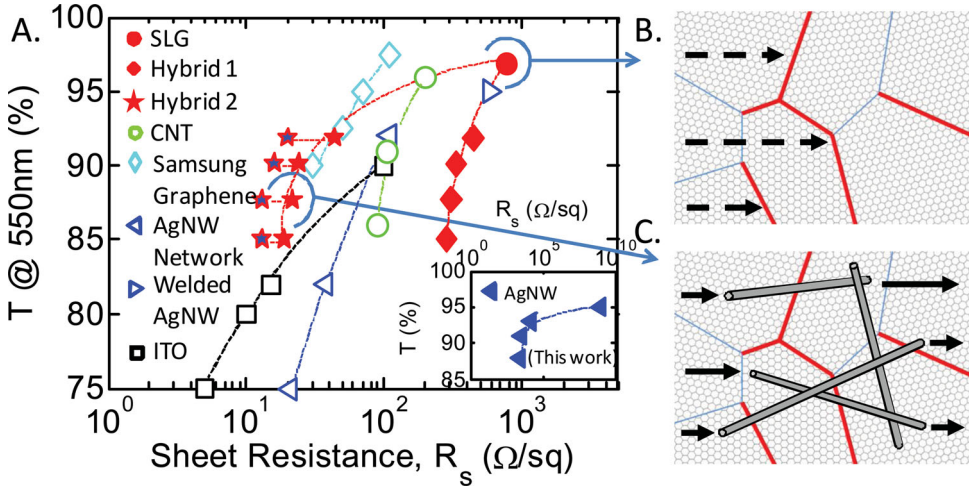

Figure 1. A) Optical transmittance at wavelength of 550 nm (T@550nm) vs. sheet resistance (R_S) for (i) previous experimental reports, including networks of carbon nanotubes,[9] networks of silver nanowires (AgNW Network and Welded AgNWs)[4,10] and ITO and (ii) measured results from this study, including CVD-grown, single-layer polycrystalline graphene (SLG), graphene/NW hybrid structures (Hybrid 1 & Hybrid 2, as described in text) with various NW densities and AgNW networks with same nominal nanowire densities (inset). Data from Hybrid 2 samples following 4 months of exposure to ambient are also shown (red stars with blue centers). The dashed lines serve as the guide to the eye. For all devices from the current study, the diffusive transmittance at 550 nm is reported. B,C) illustrate the transport across grain boundaries (GBs) in CVD SLG and hybrid SLG AgNWs networks, respectively. Low-resistance grain boundaries (LGBs, blue lines) and high-resistance grain boundaries (HGBs, red lines) are shown. The HGBs dominate the resistance in SLG. In hybrid structures with appropriate densities of AgNWs, the NWs bridge the HGBs, providing a percolating transport path for the electrons and therefore lowering the sheet resistance.

2. Results and Discussion

Here, we demonstrate a hybrid graphene/AgNW nanonet TCE with a measured R_S of 22 Ω/□ for broad-band T above 88% with a single layer of graphene (stabilized to 13 Ω/□ after four months). Representative results, including typical ITO, along with results from the current study (discussed later) are summarized in Figure 1A. The hybrid structure is shown schematically in Figure 1C and Figure 3B inset. The experiment employs commercial SLG (grain-size of ≈1 μm) with no further doping/purification/stacking. With this grain size, percolation doping (with a sub-percolation NW array) would not be expected to result in low R_S values. However, by using a NW network operating above the percolation limit, low R_S values can be obtained via co-percolating conduction, in which each sub-network (NW network and SLG) helps circumvent the transport bottleneck of the other. Consistent with this model, the overall R_S of the hybrid film is significantly smaller than the parallel combination of the two components (SLG and AgNW network). We show that the traditional approach of decorating graphene by NW (Hybrid 1) is not effective; the key to achieving low R_S is an inverted structure, where the SLG is on top of the AgNW network (Hybrid 2). In this case, more intimate contact is achieved between the graphene and NW as well as at the junctions between NWs. The optical transmittance can be explained in terms of additive absorption in the various layers. Stable electrical and optical properties of these co-percolating networks were observed even after prolonged exposure to ambient. Hybrid 2 and graphene films were also fabricated on flexible substrates; the measured resistances of the Hybrid 2 films were stable over a range of bend radii down to 8.3 mm.

The Hybrid films consisted of two components: AgNW films and SLG. Using a standard transfer recipe,[22,23] commercial CVD graphene grown on copper foil (nominally SLG and with an average grain size ≈1 μm, ACS Co., MA) was transferred onto a 1 cm × 1 cm quartz substrate (either before or after AgNW deposition). Hybrid films with two distinct configurations were fabricated corresponding to two schematics in Figure 3: Figure 3A inset shows Hybrid 1, in which the SLG was transferred to the substrate first, (AgNWs above SLG) and Figure 3B inset depicts Hybrid 2, in which the AgNW network is deposited first (AgNWs beneath SLG) (Experimental Section; Supporting information, Figure S1).

The NW networks and hybrid films contained NWs with average diameter of D_{NW}≈90 nm, average length of L_{NW}≈40 μm, and average areal densities of approximately 2×10^6, 2.8×10^6, 3.6×10^6, and 4.8×10^6 cm^{-2}, hereafter denoted as D1, D2, D3 and D4, respectively (Experimental Section; Supporting Information, Figure S1). Classical percolation theory of random sticks suggests that the percolation threshold is given by $N_C = 4.23^2/\pi L_{NW} = 3.6 \times 10^5$ cm^{-2}.[37] Although the network densities used in our measurements are significantly higher than N_C, the percolation resistance of the isolated network remains high (>1 KΩ/□, see inset of Figure 1A), reflecting poor NW-NW contact typical of such networks.[4]

Before investigating the hybrid films, we studied the crystallographic nature and average grain-size of the SLG after transfer to the quartz substrate using Raman spectroscopy and high resolution transmission electron microscopy (HRTEM).[27,38–42] **Figure 2A** shows the spectroscopic Raman mapping of CVD graphene, i.e., the spatial variation of the intensity ratios of Raman D peak (≈1350 cm^{-1}) to Raman G peak (≈1580 cm^{-1}) (I_D/I_G).[27] The D peak corresponds to the breathing mode of sp^2 hexagonal carbon but only gets activated by a defect with the help of a double resonance in the inter-valley scattering.[41] The G peak corresponds to the E_{2g} mode at the zone center of the Brillouin zone for graphitic carbon. Therefore, I_D/I_G can be used to map the grains and grain-boundaries,[27] as the grain boundaries are regions of high defect density compared to the regions within a grain. As can be seen from Figure 2A, the average grain size of our SLG is ≈1 μm. In this mapping experiment, most of the data points showed a 2D peak intensity approximately twice that of the G peak, with a Lorentzian line shape, indicating that the CVD graphene is mostly SLG throughout the film. Figure 2B shows a dark-field TEM (DF-TEM) image (Experimental Section; Supporting Information, Figure S2). The DF-TEM image at the specific spot on CVD graphene shows moiré fringes coming from the interference pattern of nearly crystallographic aligned overlapping grains. The corresponding in-plane orientation forms the diffraction pattern shown, indicating an average overlapping grain size of ≈600–800 nm. The corresponding selective area electron diffraction (SAED) image (inset) shows hexagonal symmetry.

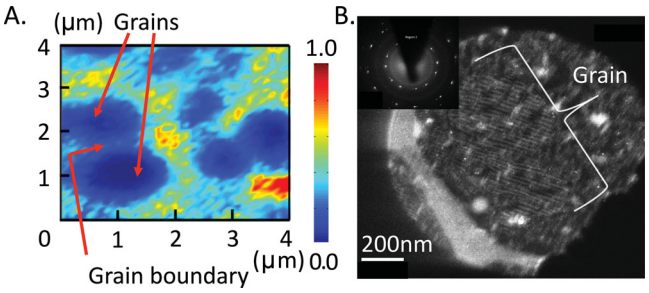

Figure 2. A) Raman spectroscopic mapping of region within SLG film. The scale bar represents (I_D/I_G) intensity ratio, with low defect density (blue) representing the grains and the high defect density (green/red) representing the grain boundaries. B) High resolution transmission electron microscopy (HRTEM) image in dark field mode. Inset shows corresponding selected area electron diffraction (SAED) pattern obtained from graphene grains. Grain size of ≈600–800 nm of two adjacent tilted grains (more prominently visible by moiré fringe) is visible.

Field-emission scanning electron microscopy (FESEM) images and the schematic representations of the two types of hybrid films are shown in **Figure 3**A,B and their insets, respectively (Hybrid 1 and Hybrid 2, respectively). In each of the FESEM images, a portion of a representative circular transfer length measurement (CTLM) device is shown; showing the metal electrodes (central and outer regions) and the hybrid structure between the electrodes. The FESEM imaging (and HRTEM imaging, discussed below) show that the structures of the two hybrids are significantly different in terms of the Graphene-NW and NW-NW interfaces. For Hybrid 1, the graphene is nominally in contact with the quartz substrate, but the NWs within the array are not in intimate contact with the graphene (nor with each other) over their entire lengths due to

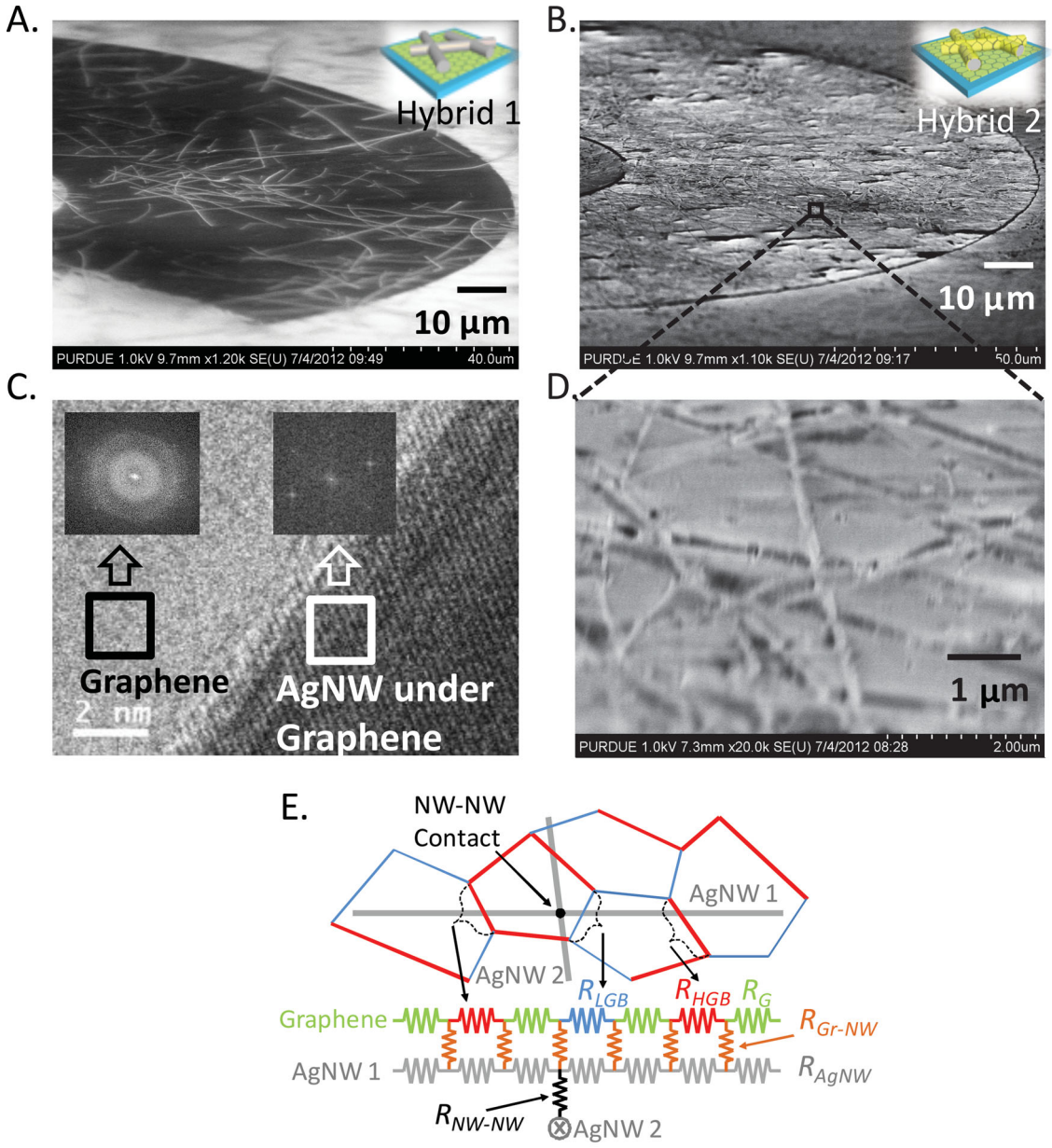

Figure 3. A,B) FESEM images and corresponding schematics (insets) of Hybrid 1 and Hybrid 2 films (defined in text) respectively, within circular transfer length measurement structures; in each case, concentric metal rings and gap where hybrid film is exposed are visible. C) HRTEM image of Hybrid 2 film, showing edge of Ag (beneath SLG) and nearby SLG region. The silver lattice planes can be clearly seen underneath the transparent SLG. D) Magnified view of FESEM image for Hybrid 2 showing the wrapping of underlying AgNWs by SLG. E) A resistor network model for graphene-AgNWs co-percolating system.

the quasi-3D stacking of the NW. For Hybrid 2, the quasi-3D stacking also exists in the NW network prior to SLG transfer. Following transfer and annealing, however, (see Experimental Section), the graphene wraps the NWs conformally, as observed in the magnified FESEM images (Figure 3D), resulting in more intimate NW to graphene contact. The force exerted by the graphene appears to compress the NW network into a more planar structure, thereby reducing $R_{NW\text{-}NW}$. The graphene/NW interface in the Hybrid 2 structure was also imaged by HRTEM (Supporting Information, Figure S2). Figure 3C shows the HR-TEM image of hybrid 2 film showing SLG-AgNW interface and wrapping of SLG over NW surface. The NW parallel lattice planes below SLG as well as the hexagonal symmetry lattice points in the reciprocal space of SLG indicates intimate contact and wrapping of SLG over NW surface.

For the SLG, AgNWs network and hybrid films, the R_S were measured using the CTLM method,[43] which relates the measured resistance R_m to R_S as follows:[44–46]

$$R_m = \frac{R_s}{2\pi R_1}[s + 2L_T] \times C.$$

Here, s is the channel length (spacing between contacts), L_T' the transfer length and R_1' the radius of the inner ring. C' is a correction factor for the circular geometry:

$$C \equiv R_1\left[\ln\left(\frac{R_1+s}{R_1}\right) + L_T\left(\frac{1}{R_1} + \frac{1}{R_1+s}\right)\right] / (s + 2L_T).$$

Several devices were measured for each channel length. Following shape correction, the corrected resistance R_t is defined as:

$$R_t = R_m / C.$$

The R_S is therefore obtained by fitting a straight line to the R_t versus s relationship, shown for SLG, Hybrid 1, and Hybrid 2 films in **Figure 4A**, using:

$$R_s = (\Delta R_t/\Delta s) \times [2\pi R_1]$$

where, $\Delta R_t/\Delta s$ is the slope and L_T is the half the 'x-intercept' of the R_t vs. s plot.

The extracted R_S versus AgNW density for the hybrid films, AgNW network, and SLG are shown in Figure 4B. Note that the SLG does not contain AgNWs, and therefore is independent of NW density. The $R_S \approx 770\ \Omega/\square$ at $T_{550nm} \approx 97\%$ (Figure 1A) is typical for relatively inexpensive, commercially available SLG, but 3× higher than best reported values.[33,36] In all other samples, the R_S decreases monotonically with increasing NW density, as expected. Hybrid 2 shows the lowest overall R_S, with R_S decreasing from 44–19 $\Omega/\square$ as the NW density is increased: at 90% transmission, $R_S \approx 24\ \Omega/\square$ for Hybrid 2 and $R_S \approx 333\ \Omega/\square$ for Hybrid 1. Figure 4B also contains a R_S value calculated from the parallel combination of the individual components (SLG ‖ AgNW): both types of hybrid films have R_S lower than this parallel combination of components, indicating conduction in the hybrid films cannot be described simply by the parallel combination of two independent conduction paths, but rather must be understood as co-percolating transport problem.

The low R_S of Hybrid 2 films can be understood by using an equivalent resistance circuit diagram (Figure 3E) to qualitatively model conduction through the 2-layer system. Figure 3E shows

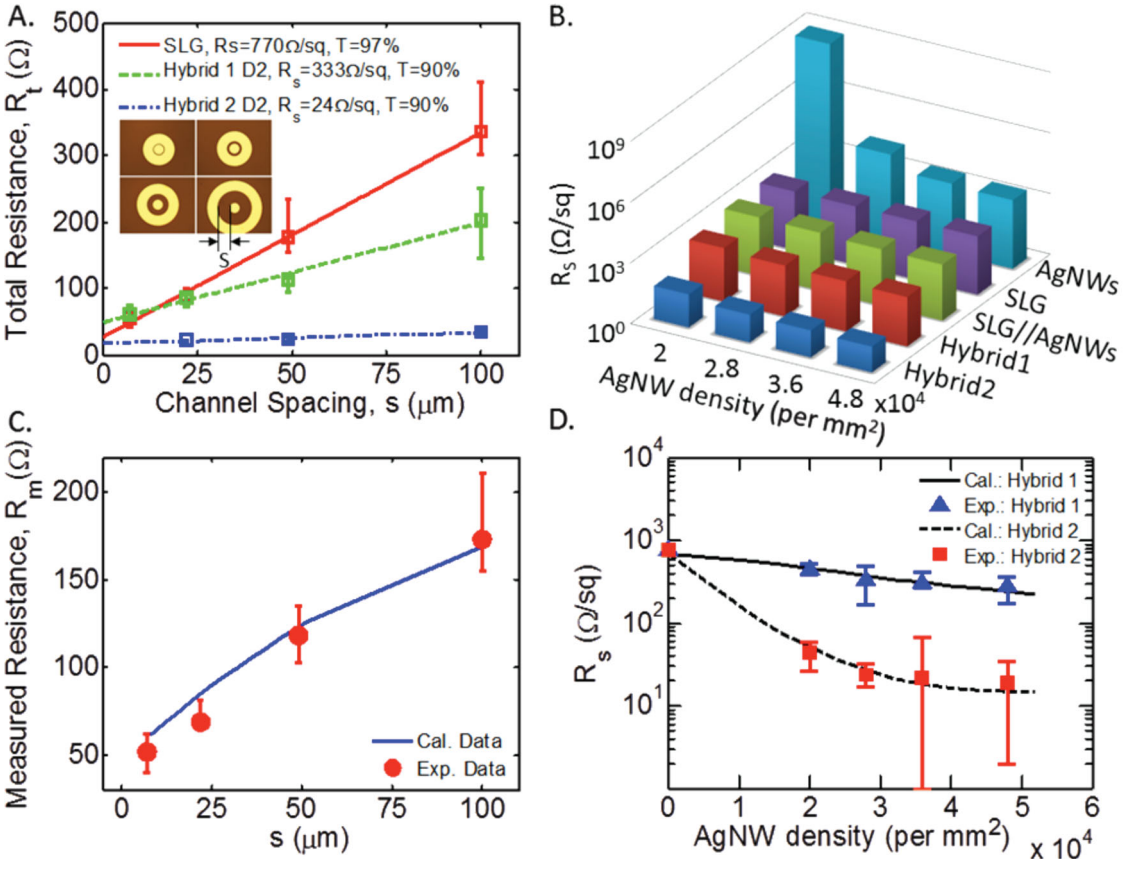

Figure 4. A) Total resistance (after correction for circular geometry) versus channel spacing for SLG, Hybrid 1 and Hybrid 2 films. Circular-TLM contact structures with four different channel spacings are shown in inset. B) Measured sheet resistance as a function of AgNW density for various samples (same legend as Figure 1). The parallel combination of measured resistances for AgNW network and SLG (labeled SLG//AgNW) is also shown for comparison. The observation of sheet resistances in the hybrid samples which are significantly lower than this parallel combination are consistent with the model in which bridges (NW-graphene contact points) link the co-percolating networks. C) Simulation results of the SLG resistance vs. channel length using one-node model[32] with $P_{GB} = 67\%$ D). Simulation result of sheet resistance of Hybrid 1 and Hybrid 2 films using approach described in text show very good agreement with experimental data.

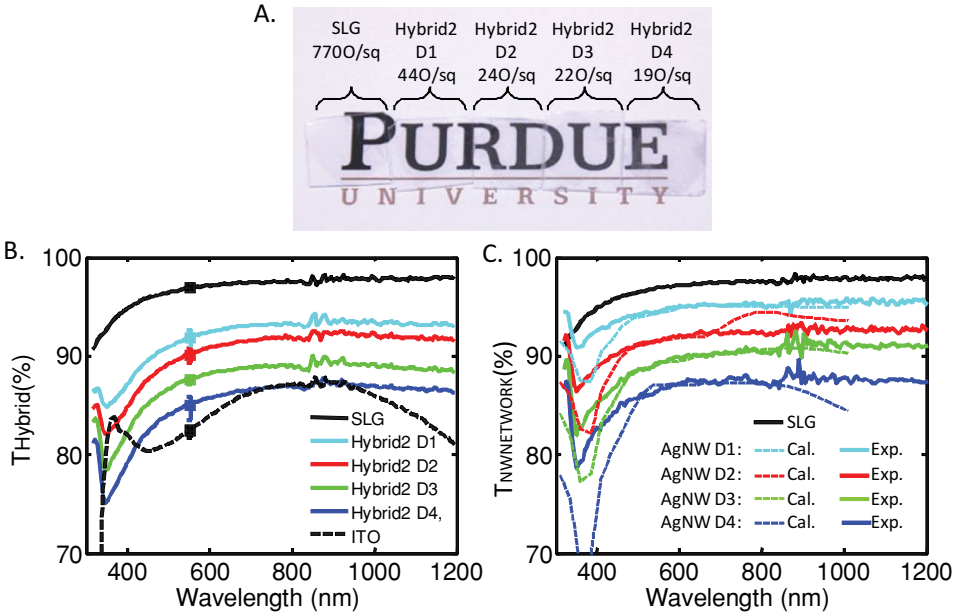

Figure 5. A) Image of quartz substrates containing SLG and Hybrid 2 films (indicated NW densities), showing high transparency (university logo is printed on white paper, kept below the samples). B) Measured diffusive transmittance spectra for SLG, Hybrid 2 films and ITO. C) Measured and simulated transmittance spectra for AgNWs networks with same AgNW densities as used in the Hybrid 2 films. Simulation is carried out for an ensemble of randomly distributed AgNWs. Absorption resonances (Supporting Information, Section S6) in periodic NW grid disappear in random distributed AgNWs).

the schematic diagram of several graphene grains separated by HGBs and LGBs, and the underneath AgNWs bridges various grain boundaries with a possible NW-NW contact region. Within the SLG film, the resistances of grain boundaries (R_{HGB} and R_{LGB} for HGBs and LGBs, respectively) dominate the R_S. Within the NW network only, the R_S is dominated by $R_{NW\text{-}NW}$, which will vary with contact geometry and external pressure, but is typically much larger than the resistance through an individual NW (R_{NW}). In the hybrid films, the two layers are coupled by a graphene-NW contact resistance ($R_{Gr\text{-}NW}$). Various transport paths are indicated by arrows in the Supporting Information, Section S4. A detailed theoretical analysis of this co-percolation problem is discussed later.

As illustrated qualitatively in **Figure 5A**, the T of the SLG and hybrid films are relatively high, and decreases monotonically as the NW density is increased from D1-D4. For reference, the corresponding R_S values are stated. The optical transmittance spectra of SLG and hybrid films (on unpatterned quartz substrates), were measured at normal incidence in specular and diffusive mode (Experimental Section; Supporting Information, Section S5). The measured spectra were corrected with transmittance of a bare quartz substrate.

As shown in Figure 5B, our SLG film shows T_{550nm} ≈97% and T almost independent of wavelength. This is consistent with reported optical absorption of 2.3% per layer of graphene.[21] Below 500 nm, the roll-off in absorption is sometimes attributed to hydrocarbon contamination or a surface plasmon tail broadened by the contamination. Figure 5B also shows the measured T for various Hybrid 2 films for NW densities of D1, D2, D3, and D4: the T_{550nm} (averaged over five different locations) decreases almost linearly (97%, 92.6%, 90%, 87.3% and 85.1%) with NW density. Within a given sample, point-to-point variations are small (<1% typically), indicating relatively uniform densities of NWs throughout a sample. These T_{550nm} values for the respective samples are utilized in Figure 1A. For our hybrid films, the diffusive T is slightly higher than the specular T and this difference increases with increasing NW density (Experimental Section; Supporting Information, Section S5), a desirable feature for TCEs for optoelectronic and photovoltaic devices.[47] Finally, for comparison, the T of an ITO film is also plotted in Figure 5B, indicating inferior transmission and well-known roll-off at higher wavelengths.

To understand the relative contributions to T for SLG and NW-network, the measured T versus wavelength for AgNW networks with the same nominal NW densities used in the hybrid structures (but without SLG) is shown in Figure 5C. For comparison, the curve for SLG is repeated in this figure. By comparing Figure 5B,C, one can see that the overall transmittance of the hybrid is approximately equal to the product of respective transmittances of the two layers, i.e., $T_{Hybrid} = T_{SLG} \times T_{NW\text{-}network}$. The measured $T_{NW\text{-}network}$ is consistent with prior studies of random silver NW networks.[4,48]

The numerical solution of 3D Maxwell's equation through a randomly distributed AgNW with densities D1-D4 (L_{NW} = 40 μm and D_{NW} = 90 nm) interprets, with no fitting parameters, three distinctive features of $T_{NW\text{-}network}$ as follows. First, the dip in T for 350 nm<λ<400 nm can be attributed to the local surface plasmon resonance (LSPR) of silver.[47] Second, the smoothness of T for λ>600 nm reflects averaging of random phases associated with the disordered network (Experimental

Section; Supporting Information, Section S6). Finally, the empirically observed linear decrease in T with NW densities (solid line, Figure 5C) is reproduced quantitatively in the simulation (dashed line, Figure 5C) – clearly establishing a trade-off between percolation doping and optical transmission.

Several thermal/mechanical techniques such as tungsten lamp welding[10] and carbon nanotube bridging[34] have been reported to reduce relatively large R_S of AgNW networks primarily arising from large $R_{NW\text{-}NW}$. The electrical robustness of our Hybrid 2 samples and AgNW network was further studied by re-measuring the electrical properties following application of uniform mechanical pressure (with a relative stress of ≈ 100 kPa between the pressing surfaces) on the substrate containing the CTLM devices. The R_S of the AgNW network was reduced by a factor of three whereas the hybrid films show no change in their R_S values. This is consistent with a picture in which $R_{NW\text{-}NW}$, the most resistive component of the percolative path in the AgNW network, is improved after applying pressure. For hybrid films, the high-resistance NW-NW junctions are already circumvented by graphene; therefore, any change in NW-NW resistance due to mechanical pressure is not reflected in the overall resistance. The environmental stability of the hybrid films was evaluated by re-measuring the electrical properties following exposure to ambient for 4 months. Hybrid 2 devices exhibited a reduced R_S and no significant degradation in measured T (Figure 1A). The lowest value of R_S was 13 Ω/□ (vs. 22 Ω/□ prior to ambient exposure), with T_{550nm}≈88% in Hybrid 2 films with AgNW concentrations D3 (Experimental Section; Supporting Information, Section S7). Hybrid 1 devices also exhibited modest improvements in R_S, but the T decreased following ambient exposure. The different behavior in the two hybrid types is believed to be due to the graphene sheet acting as a diffusion barrier for atmospheric gases in Hybrid 2, which likely retards oxidation of the AgNWs. SLG and Hybrid 2 films (with similar CTLM devices) were fabricated on flexible poly(ethylene terephthalate) (PET) substrates. The resistances of the samples were chararacterized at various bend radii ranging from semi-infinity (flat substrate) to 8.3 mm. Compared to SLG, Hybrid 2 films show excellent stability over various degrees of bending (Experimental Section; Supporting Information, Section S8).

We have previously proposed the concept of 'percolation doping' in hybrid SLG/NW systems where the conductivity can be improved (with respect to SLG with typical grain sizes) while preserving high transparency, by bridging the HGBs using metallic NWs.[32] Unlike chemical doping, this approach increases conductivity by providing conduction channels through NWs which connect grains that had previously been isolated by HGBs. The experimental result presented in Figure 4 (and summarized in Figure 1A) serves as a proof-of-concept of a more generalized version of percolation doping of SLG grains by NWs. In this copercolating system, the transport bottleneck of one component (e.g., AgNW) is circumvented by the transport channels of the other (e.g., graphene) and vice versa. Although R_S of Hybrid 1 and 2 can both be understood by copercolating transport, the lower R_S in Hybrid 2 is attributed to the more intimate contact (and therefore, reduced $R_{Gr\text{-}NW}$ and $R_{NW\text{-}NW}$) associated with the wrapping of the SLG over the NWs. The spontaneous wrapping of graphene over metallic nanoparticle surface (in our case, AgNWs) is energetically favored and is shown recently by Li et al. using molecular dynamics simulation.[49]

For a quantitative interpretation and to determine the fraction of HGBs in SLG film, we calculate the R_S of poly-graphene using a "one-node" random-network percolation model, as follows (the model is validated in ref. [32], see Supporting Information, Section S4). In a one-node model, the SLG is represented by a 2D network of grains, each represented by an intra-grain resistance (R_G ≈150 Ω) corresponding to a grain-size (D_G) of ≈1 μm, typical ratio of inter-grain to intra-grain resistances R_{HGB}/R_{LGB} ≈10,[17,21] R_{LGB}/R_G ≈1. An ensemble average over 500 samples (with fraction of high-resistance grain-boundaries, P_{GB} = 67%)[29] offers consistent interpretation of circular TLM resistances (Figure 4C).

To obtain the R_S for Hybrid 1 and 2, the one-node model must now include a parallel network incorporating the self-resistances of NW (R_{NW}≈15 Ω), junction resistance of $R_{NW\text{-}NW}$ = 1 GΩ, and densities D1-D4. This NW-network is connected at random points to SLG by $R_{Gr\text{-}NW}$, with different values for Hybrid 1 and Hybrid 2. In interpreting the results of Hybrids 1 and 2, the co-percolating resistor network model suggests that approximately 1/3 of the NWs make contact with the SLG. This is consistent with the quasi-three dimensional NW networks observed in the images, which make it unlikely that all the NWs are in physical contact with the SLG sheet. Of the NWs that do contact graphene, Hybrid 1 is characterized by $R_{Gr\text{-}NW}$ ≈550 Ω, as is typical for weakly coupled NW-graphene network.[50] On the other hand, the behavior of Hybrid 2 is best interpreted by $R_{Gr\text{-}NW}$≈0 Ω, reflecting the importance of wrapping of NW by SLG. Independent recent experiments[51] have attributed this vanishingly small $R_{Gr\text{-}NW}$ to 'chemical' doping of SLG by charge transfer from AgNWs. We believe that the anneal-induced doping of graphene by AgNWs is more effective for Hybrid 2, due to intimate wrapping of AgNW by SLG. (Figure 3B–D).

3. Conclusions

In conclusion, we have developed an approach for realizing high performance TCEs consisting of hybrid assemblies of graphene and silver nanowire networks of varying densities. A R_S of 22 Ω/□ was obtained in our hybrid films at 88% optical transparency (stabilized to 13 Ω/□ after four months), with excellent stability upon atmospheric exposure, mechanical pressure and mechanical bending. These TCE properties are better than commercially-available ITO and comparable to the best reported results in TCEs. A rigorous modeling study provides a model for the co-percolating conduction, in which the high-resistance grain boundaries in graphene are bridged by the AgNWs, and high-resistance junctions between NWs in a NW-network are bridged by graphene, resulting in a low R_S even at modest NW densities. The low R_S can be attributed to grain boundary engineering, rather than to conduction through the AgNW networks. Our method could readily provide a route towards low-cost approaches for realizing high performance TCEs in various kinds of optoelectronic and photovoltaic devices involving 2D and 1D nanostructure.

4. Experimental Section

Fabrication Processes for SLG and Hybrid Films: Commercial CVD SLG on copper foil (ACS Materials Co., MA) was employed. Standard procedures[22] were followed for plasma etching of SLG from back side of Cu and layer transfer onto a 1 cm × 1 cm quartz substrate (SPI Supplies, PA), including copper etching using iron nitrate solution. Commercial AgNWs (Blue Nano Inc., NC), with diameters of 70–110 nm and lengths of 20–60 μm, are dispersed in isopropyl alcohol at a concentration of 0.1 mg mL^{-1}. AgNW networks were drop cast either after (Hybrid 1) or before (Hybrid 2) SLG transfer, with density controlled by number of drops. Finally, the hybrid films were annealed for 1 h in forming gas at 300 °C with a 40 sccm flow rate. The schematic process flow of SLG transfer and fabrication of hybrid films is shown in Supporting information, Figure S1. SLG and Hybrid 2 films were also fabricated on transparent, flexible PET substrates (from Dupont) for mechanical bending tests.

Raman Mapping, FESEM, and HRTEM Measurements: The Raman spectra and Raman spatial mapping were performed using a Raman spectrometer (Horiba Jobin Yvon Model Xplora with a confocal microscope and motorized sample stage) in a back-scattered geometry with a CCD detector and 532 nm excitation source. The laser spot size was ≈0.6 μm with a 100× objective lens with numerical aperture (NA) of 0.9. Using a pixel size of 0.2 μm × 0.2 μm, multiple 6 μm × 6 μm regions were mapped. The spectral resolution was 2.5 cm^{-1} (corresponding to grating with 1200 grooves per mm), and each spectrum was averaged over three acquisitions of 5 s each. The spectra were baseline corrected and fitted with Lorentzian line shape for evaluating peak intensities and positions. FESEM images were taken in secondary electron mode using a Hitachi S4800, with accelerating voltage below 1 kV to minimize electron beam-induced damage. TEM images were taken using a FEI Titan environmental HRTEM at an accelerating voltage of 80–100 kV (Supporting Information, Figure S2). Selected area electron diffraction (SAED) patterns were extracted from fast Fourier transform (FFT) analysis using the Image J software. DF-TEM images were taken at 80 kV, with the electron beam blocked by a 30 μm objective aperture filter around each of the equivalent diffraction peaks. A procedure comparable to that recently reported for highlighting grains using DF-TEM[25] was employed.

Device Fabrication and Electrical Measurement: CTLM electrode with channel lengths of ≈7, 22, 49 and 100 μm were fabricated by evaporation of Ti/Pd/Au (thickness 1 nm/30 nm/20 nm) in a Kurt J. Lesker electron-beam evaporator with base pressure of ≈9 × 10^{-7} Torr, followed by lift-off. Two-terminal current vs. voltage measurements were performed using a probe station (Cascade Microtech.), Keithley 7174A switch matrix system, and a Keithley 4200 SCS semiconductor parameter analyzer. Sheet resistances were measured using CTLM[43], with geometry correction before sheet resistance calculation.[44–45] Figure S3, Supporting Information, shows (i) the circular TLM pattern used for the devices, (ii) statistical distribution of the measured data, and (iii) final fitting of the curve to extract the sheet resistance of SLG, Hybrid 1 and Hybrid 2 (corresponding to AgNW density of D4). In calculating the ensemble average, we have excluded a very small fraction (less than 10%) of 'outlier' devices whose sheet resistance deviated more than 50% from the ensemble mean, indicating damaged SLG and/or improper processing.

Specular and Diffusive Transmittance: Since the surfaces of the hybrid films are textured, it is important to characterize their diffusive and specular transmittances. The diffusive spectra for the (i) quartz substrate, (ii) quartz with SLG, and (iii) the quartz with hybrid films were all measured at normal incidence using a Perkin Elmer (lambda 950) UV/VIS/NIR spectrophotometer. The instrument was first calibrated with standard spectralon plate reference corresponding to 100% transmittance, and the measurements were made in 300–1200 nm wavelength range with data taken at each 5 nm interval. The specular measurements were made using a Cary 5G UV/VIS/NIR spectrophotometer over the same wavelength range at normal incidence. As shown in supporting information (Supporting Information, Section S5, Figure S7), the difference between both transmittance increases with nanowire density, as expected.

Optical Simulation for AgNWs: A 2D approximation of the AgNWs structure (without SLG) was used to model (by solving the 3D Maxwell's equations numerically) the optical response of the AgNWs nanonet structure used in Hybrid 1 and Hybrid 2. Numerical study using COMSOL RF-module and MATLAB were used for both transverse electric (TE) and transverse magnetic (TM) waves (Supporting Information, Section S6).

Mechanical Stress and Chemical Stability: Mechanical pressure was applied on the devices with AgNWs, as well as the devices with hybrid films by pressing the CTLM devices. Electrical measurements were performed just after applying the pressure. The chemical stability of the hybrid samples were assessed by storing the devices over four months in nitrogen-filled glove-box, then exposing the devices to normal atmospheric condition for 4–5 days, and finally, measuring the sheet resistance at the end of the period. The details of the measurement results are given in Supporting Information, Section S7. For the mechanical bending test, the SLG and Hybrid 2 films were wrapped over the surfaces of half-cylindrical forms of radii 14.6 mm, 11.5 mm, and 8.3 mm respectively and the CTLM devices with channel length of 100 μm were electrically probed (Supporting Information, Section S8).

Supporting Information

Supporting Information is available from the Wiley Online Library or from the author.

Acknowledgements

R.C. and S.R.D. contributed equally to this work. We acknowledge Prof. Y. P. Chen and L. Jauregui for providing Raman Spectroscopy measurement facility and sharing the matlab code, respectively. Authors thank M. Cem Akatay, Y. Zhi for helping in HRTEM measurements, and Dr. Debashis Chanda (University Illinois at Urbana Champaign) for carrying out specular transmittance measurements. This work was supported as part of the Center for Re-Defining Photovoltaic Efficiency Through Molecule Scale Control, an Energy Frontier Research Center (EFRC) funded by the U.S. Department of Energy, Office of Science, Office of Basic Energy Sciences under Award Number DE-SC0001085.

Received: December 30, 2012
Revised: March 10, 2013
Published online: April 25, 2013

[1] C. G. Granqvist, A. Hultaker, *Thin Solid Films* **2002**, *411*, 1.
[2] T. Minami, *J. Vac. Sci. Technol.* **1999**, *A17*, 1765.
[3] X. Jiang, F. L. Wong, M. K. Fung, S. T. Lee, *Appl. Phys. Lett.* **2003**, *83*, 1875.
[4] L. Hu, H. S. Kim, J. Y. Lee, P. Peumans, Y. Cui, *ACS Nano* **2010**, *4*, 2955.
[5] V. Scardaci, R. Coull, J. N. Coleman, *Appl. Phys. Lett.* **2010**, *97*, 023114.
[6] L. Hu, D. S. Hecht, G. Gruner, *Nano Lett.* **2004**, *4*, 2513.
[7] N. Pimparkar, M. A. Alam, *IEEE Elect. Dev. Lett.* **2008**, *29*, 1037.
[8] S. Kumar, J. Y. Murthy, M. A. Alam, *Phys. Rev. Lett.* **2005**, *95*, 066802.
[9] H. Geng, K. K. Kim, K. P. So, Y. S. Lee, Y. Chang, Y. H. Lee, *J. Am. Chem. Soc.* **2007**, *129*, 7758.
[10] E. C. Garnett, W. Cai, J. J. Cha, F. Mahmood, S. T. Connor, M. G. Christoforo, Y. Cui, M. D. McGehee, M. L. Brongersma, *Nat. Mater.* **2012**, *11*, 241.

[11] A. R. Madaria, A. Kumar, F. N. Ishikawa, C. Zhou, *Nano Res.* **2010**, *3*, 564.
[12] H. Wu, L. Hu, M. W. Rowell, D. Kong, J. J. Cha, J. R. McDonough, J. Zhu, Y. Yang, D. McGehee, Y. Cui, *Nano Lett.* **2010**, *10*, 4242.
[13] J. Y. Lee, S. T. Connor, Y. Cui, P. Peumans, *Nano Lett.* **2008**, *8*, 689.
[14] W. Gaynor, G. F. Burkhard, M. D. McGehee, P. Peumans, *Adv. Mater.* **2011**, *23*, 2905.
[15] R. Zhu, C.-H. Chung, K. C. Cha, W. Yang, Y. B. Zheng, H. Zhou, T.-B. Song, C.-C. Chen, P. S. Weiss, G. Li, Y. Yang, *ACS Nano* **2011**, *5*, 9877.
[16] K. S. Novoselov, A. K. Geim, S. V. Morozov, D. Jiang, Y. Zhang, S. V. Dubonos, I. V. Grigorieva, A. A. Firsov, *Science* **2004**, *306*, 666.
[17] K. S. Novoselov, A. K. Geim, S. V. Morozov, D. Jiang, Y. Zhang, S. V. Dubonos, I. V. Grigorieva, A. A. Firsov, *Nature* **2005**, *438*, 197.
[18] Y. Zhang, Y. W. Tan, H. L. Stormer, P. Kim, *Nature* **2005**, *438*, 201.
[19] A. K. Geim, K. S. Novoselov, *Nat. Mater.* **2007**, *6*, 183.
[20] F. Schedin, A. K. Geim, S. V. Morozov, E. W. Hill, P. Blake, M. I. Katsnelson, K. S. Novoselov, *Nat. Mater.* **2007**, *6*, 652.
[21] R. R. Nair, P. Blake, A. N. Grigorenko, K. S. Novoselov, T. J. Booth, T. Stauber, N. M. Peres, A. K. Geim, *Science* **2008**, *320*, 1308.
[22] X. Li, W. Cai, J. An, S. Kim, J. Nah, D. Yang, R. Piner, A. Velamakanni, I. Jung, E. Tutuc, S. K. Banerjee, L. Colombo, R. S. Ruoff, *Science* **2009**, *324*, 1312.
[23] X. Li, R. S. Ruoff, *Nano Lett.* **2009**, *9*, 4359.
[24] K. S. Kim, Y. Zhao, H. Jang, S. Y. Lee, J. M. Kim, K. S. kim, J. H. Ahn, P. Kim, J. Choi, B. H. Hong, *Nature* **2009**, *457*, 706.
[25] P. Y. Huang, C. S. R. Vargas, A. M. Van der Zande, W. S. Whitney, M. P. Levendorf, J. W. Kevek, S. Garg, J. S. Alden, C. J. Hustedt, Y. Zhu, J. Park, P. L. McEuen, D. A. Muller, *Nature* **2011**, *469*, 389.
[26] A. W. Tsen, L. Brown, M. P. Levendorf, F. Ghahari, P. Y. Huang, R. W. Havener, C. S. Ruiz-Vargas, D. A. Muller, P. Kim, J. Park, *Science* **2012**, *336*, 1143.
[27] Q. Yu, L. A. Jauregui, W. Wu, R. Colby, J. Tian, Z. Su, H. Cao, Z. Liu, D. Pandey, D. Wei, T. F. Chung, P. Peng, N. P. Guisinger, E. A. Stach, J. Bao, S. Pei, Y. P. Chen, *Nat. Mater.* **2011**, *10*, 443.
[28] A. Hashimoto, K. Suenaga, A. Gloter, K. Urita, S. Iijima, *Nature* **2004**, *430*, 870.
[29] Y. Wei, J. Wu, H. Yin, X. Shi, R. Yang, M. Dresselhaus, *Nat. Mater.* **2012**, *11*, 759.
[30] P. Kim, *Nat. Mater.* **2010**, *9*, 792.
[31] O. V. Yazyev, S. G. Louie, *Nat. Mater.* **2010**, *9*, 806.
[32] C. Jeong, P. Nair, M. Khan, M. Lundstrom, M. A. Alam, *Nano Lett.* **2011**, *11*, 5020.
[33] R. Chen, S. R. Das, C. Jeong, D. B. Janes, M. A. Alam, *Proc. 70th IEEE Device Research Conf. (DRC)*, 18-20 June 2012, Penn State; DOI: 10.1109/DRC.2012.6257034.
[34] V. C. Tung, L. Chen, M. J. Allen, J. K. Wassei, K. Nelson, R. B. Kaner, Y. Yang, *Nano Lett.* **2009**, *9*, 1949.
[35] I. N. Kholmanov, C. W. Magnuson, A. E. Aliev, H. Li, B. Zhang, J. W. Suk, L. L. Zhang, E. Peng, S. H. Mousavi, A. B. Khanikaev, R. Piner, G. Shvets, R. S. Ruoff, *Nano Lett.* **2012**, *12*, 5679.
[36] S. Bae, H. Kim, Y. Lee, X. Xu, J. Park, Y. Zheng, J. Balakrishnan, T. Lei, H. R. Kim, Y. I. Kim, K. S. Kim, B. Ozyilmaz, J. Ahn, B. H. Hong, S. Iijima, *Nat. Nanotechnol.* **2010**, *5*, 574.
[37] G. E. Pike, C. H. Seager, *Phys. Rev. B* **1974**, *10*, 1421.
[38] A. C. Ferrari, J. C. Meyer, V. Scardaci, C. Casiraghi, M. Lazzeri, F. Mauri, S. Piscanec, D. Jiang, K. S. Novoselov, S. Roth, A. K. Geim, *Phys. Rev. Lett.* **2006**, *97*, 187401.
[39] M. S. Dresselhaus, A. Jorio, M. Hofmann, G. Dresselhaus, R. Saito, *Nano Lett.* **2010**, *10*, 751.
[40] A. Das, S. Pisana, B. Chakraborty, S. Piscanec, S. K. Saha, U. V. Waghmare, K. S. Novoselov, H. R. Krishnamurthy, A. K. Geim, A. C. Ferrari, A. K. Sood, *Nat. Nanotechnol.* **2008**, *3*, 210.
[41] M. A. Pimenta, G. Dresselhaus, M. S. Dresselhaus, L. G. Cancado, A. Jorio, R. Saito, *Phys. Chem. Chem. Phys.* **2007**, *9*, 1276.
[42] T. M. G. Mohiuddin, A. Lombardo, R. R. Nair, A. Bonetti, G. Savini, R. Jalil, N. Bonini, D. M. Basko, C. Galiotis, N. Marzari, K. S. Novoselov, A. K. Geim, A. C. Ferrari, *Phys. Rev.* **2009**, *B79*, 205433.
[43] S. S. Cohen, *VLSI electronics* vol. *13*, Academic Press, London, **1986**, ISBN 0-12-234113-9.
[44] G. K. Reeves, H. B. Harrison, *IEEE Electron Device Lett.* **1982**, *3*, 111.
[45] J. H. Klootwijk, C. E. Immering, *Proc. IEEE Int. Conf. on Microelectronic Test Structures* **2004**, *17*, 247.
[46] B. Jacob, M. C. J. C. M. Kramer, E. J. Geluk, F. Karouta, *J. Crystal Growth* **2002**, *241*, 15.
[47] J. van de Groep, P. Spinelli, A. Polman, *Nano Lett.* **2012**, *12*, 3138.
[48] S. De, T. M. Higgins, P. E. Lyons, E. M. Doherty, P. N. Nirmalraj, W. J. Blau, J. J. Boland, J. N. Coleman, *ACS Nano* **2009**, *3*, 1767.
[49] Y. F. Li, H. Q. Yu, H. Li, C. G. An, K. Zhang, K. M. Liew, X. F. Liu, *J. Phys. Chem.* **2011**, *C115*, 6229.
[50] A. Hsu, *IEEE Electron Device Lett.* **2011**, *32*, 1008.
[51] R. Nouchi, T. Saito, K. Tanigaki, *J. Appl. Phys.* **2012**, *111*, 084314.